

Calibrated electrorotation for characterizing the torque generation by individual flagellar motors

Kento Sato¹, Shuichi Nakamura¹, Seishi Kudo¹, and Shoichi Toyabe^{1,*}

¹Department of Applied Physics, Graduate School of Engineering, Tohoku University, Sendai 980-8579, Japan

*Correspondence: toyabe@tohoku.ac.jp

ABSTRACT Bacterial flagellar motor is one of the most complex and sophisticated nano machineries in nature. A torque-speed curve indicates the performance of a motor and contains fruitful information about its torque generation mechanism. However, a precise measurement of the torque-speed characteristic of a single flagellar motor is still challenging. With the conventional methods based on the beads assay, the characteristics of individual motors are lost due to the averaging of multiple torque-speed curves. This limits the detailed modelling of the rotation mechanism. Here, we demonstrate to measure the torque-speed relationship of individual flagellar motors of *Salmonella* under dynamically-controlled external load by a calibrated electrorotation method. The obtained torque-speed curves have a steep rise near the stall, indicating the presence of a barrier to reverse the rotation.

Calibrated electrorotation for characterizing the torque generation by individual flagellar motors

Kento Sato¹, Shuichi Nakamura¹, Seishi Kudo¹, and Shoichi Toyabe^{1,*}

¹Department of Applied Physics, Graduate School of Engineering, Tohoku University, Sendai 980-8579, Japan

*Correspondence: toyabe@tohoku.ac.jp

1 INTRODUCTION

Despite the intensive studies on the bacterial flagellar motor, its rotation mechanism remains to be elucidated (1–3). For example, a fundamental question such as how its stator converts ion motive force (IMF) to torque has not yet been answered clearly.

Precise measurement of a torque-speed (TS) characteristic is central to elucidate the rotation mechanism of motors. The TS curve helps to infer the torque generation mechanism; whether the torque is generated by a power-stroke type or a ratchet type mechanism (4). In addition, the fact that the dynamical torque control by the motor based on a stator-number change depends on IMF (5), coupling ion (6), and load (5, 7) demands to measure the response of the motor output to a dynamic perturbation of such factors.

In this work, we demonstrate to measure the TS curves of individual motors of *Salmonella* on the basis of a calibrated electrorotation method. The method applies dynamic torque with a calibrated magnitude on a tethered cell (Fig. 1a). By sweeping the external torque while measuring the rotational trajectory, we recovered the TS curves ranging from the stall to the zero-load conditions. In the following, after briefly describing the limitations of the conventional beads assay, we will elaborate on the methodology of the calibrated electrorotation method.

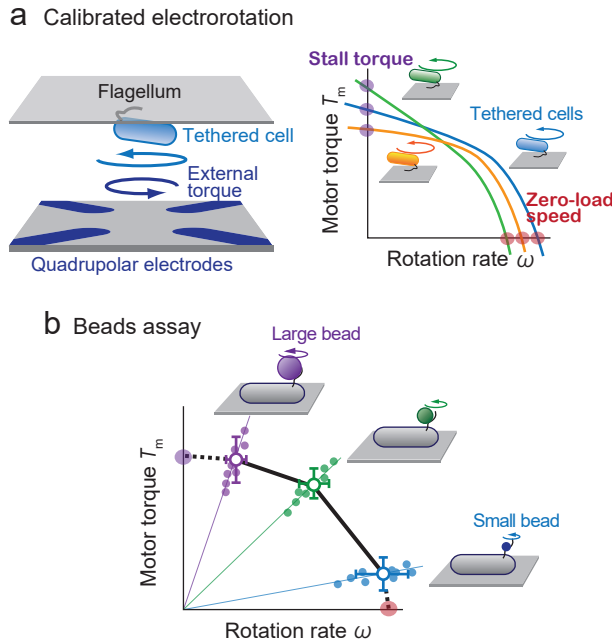


Figure 1: **a**, Calibrated electrorotation method provides torque-speed curves of individual motors in a broad range including the reversed rotation and the negative motor torque. **b**, Beads assay averages out the torque-speed characteristics of individual motors. Filled circles correspond to the motor torque estimated for individual motors. Torque -speed curve is obtained by connecting the average under each condition (open circles). The stall torque and zero-load speed are obtained by an extrapolation.

1.1 Beads assay

A basic idea of the TS curve measurement is to measure the rotation speed under a load of a known magnitude. Beads assay is a standard technique to measure the TS curves (3, 8–13). The motor rotation was probed by a micron- or submicron-sized particle attached to a flagellum of a cell fixed on a glass surface (Fig. 1b). By combining probes of various sizes and buffer of various viscosity, a viscous load in a broad range of magnitude is imposed on the motor. Because inertia is negligible in such microscopic systems, the torque generated by the motor $T_m(\omega)$, the viscous torque loaded on the motor $\gamma\omega$, and the thermal fluctuating torque are balanced. Here, γ is the rotational frictional coefficient felt by the motor and contains the contributions from the probe bead, flagellar filament, and the internal friction of the motor. ω is the rotational rate. The thermal fluctuation is negligible when averaged in a sufficiently long time period. Therefore, by estimating γ properly and measuring ω , the motor torque is obtained as

$$T_m(\omega) = \gamma\omega. \quad (1)$$

The method is simple and has been widely used. However, there are mainly three limitations on this method. (i) The TS curve of an individual motor can be obtained by monitoring rotation of a single motor while changing viscosity of a buffer, but it is discontinuous and laborious (10, 14, 15). Instead, the torque of multiple motors is averaged under each condition in most experiments (Fig. 1b). This averages out the torque characteristics of individual motors and poses a limitation on the construction of a detailed rotation model. It also prevents a systematic study of the load dependency of the stator number dynamics (5, 7).

(ii) Viscous load cannot reverse the rotation nor assist the rotation in principle. A stall torque, the external torque necessary to reverse the rotation, and a zero-load speed, the rotation rate free from load, are key quantities to characterize the TS curve. In the beads assay, they are obtained only by an extrapolation (12, 16).

(iii) Estimation of γ is not solid (14). γ is calculated based on the geometric parameters of the probe-flagellum complex. An often used equation (11) is

$$\gamma = \frac{2\pi L r_f^2 (2p^2 + 4\pi^2 r_f^2) \eta}{(p^2 + 4\pi^2 r_f^2)(\ln(2p/d) - 0.5)} + 8\pi\eta r^3 + 6\pi\eta r R^2. \quad (2)$$

Here, L , d , and p are the length, radius, and pitch of the flagellar filament, respectively. r_f is the spiral radius. r and R are the bead radius and the rotation radius of the bead, respectively. However, precise values of the filament length L and probe size r are not known, making a large estimation error of γ due to the cubic dependence of γ on r . In addition, the friction of the probe close to the cell surface is complicated due to the hydrodynamic effect (17).

1.2 Electrorotation method

Alternatively, the electrorotation method imposes an external torque with a controlled magnitude to a microscopic dielectric object by inducing high-frequency alternative current (AC) electric field. The method was applied to the tethered bacterial cells (8, 18–23) (Fig. 1a). Because the torque magnitude is proportional to the square of the applied voltage amplitude V_0 , the load on a motor can be dynamically and continuously controlled by modulating V_0 .

Despite these advantages, the method is not widely used mainly due to a lack of the torque calibration method. The motor torque T_m under the electrorotation becomes

$$T_m(\omega) = \gamma\omega - \alpha_0 V_{sq}, \quad (3)$$

where $\alpha_0 V_{sq}$ is an external torque with $V_{sq} = V_0^2$ or $-V_0^2$ depending on the sign of the phase shift of the applied AC voltages. The coefficient α_0 depends on multiple factors including the cell shape, the chamber geometry, and the dielectric properties of the cell body and the buffer. Therefore, it is not possible to determine α_0 *a priori*. This has hampered the use of the electrorotation method to measure the TS curve. In the previous papers (8, 19–23), “relative” external torque instead of the exact torque magnitude has been used to plot the torque characteristic.

1.3 Calibration of electrorotation torque

Previously, we have established a torque calibration method of the electrorotation method. The method was successfully applied to F₁-ATPase motor and revealed its torque characteristics (24–27). The method provides not only α_0 but also γ *in situ* without any knowledge about the geometry of the probe-motor complex, implementing a methodology to recover the precise torque characteristics of individual motors (Fig. 2).

The calibration is based on the fluctuation-response relation, which relates the thermal fluctuation to the response to external perturbation under a condition close to the equilibrium (28, 29). Because the motor’s rotation is limited to a low frequency region and settled at equilibrium at high frequencies, the calibration is possible by comparing the rotational fluctuation and response of rotation against external perturbation at the high frequency.

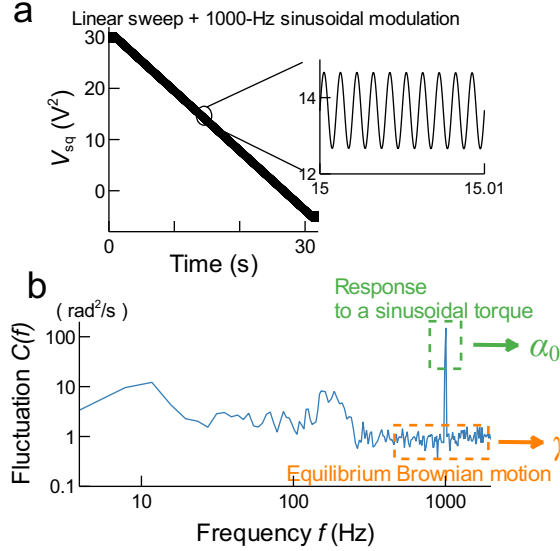


Figure 2: Experimental procedure. **a**, Typical voltage profile. V_{sq} was varied from negative to positive at a constant rate with one-second pauses before and after the ramp. The range and duration of ramps varied among experiments. A 1000-Hz sinusoidal voltage with amplitude of typically between 0.5 and 2 V^2 was superposed to measure the response. **b**, Fluctuation spectrum of the rotation rate $C_r(f)$. A steep peak at 1000 Hz corresponds to the response to a sinusoidal probe torque induced for the torque calibration. γ is obtained from the spectrum height at the frequencies close to 1000 Hz (10). α_0 is obtained from the 1000-Hz peak height and γ (10). See Methods for details.

Here, we developed the calibration method and applied it to the tethered cell assay of *Salmonella* (See Methods section for details). However, the application of this method to the flagellar motors is not straightforward and needs some modifications. The flagellar motor rotates much faster than F_1 -motor and produces nonequilibrium fluctuations at relatively high frequencies. These nonequilibrium fluctuations are superposed on the equilibrium Brownian spectrum and impedes the torque calibration. As we will see, we suppressed the nonequilibrium fluctuations dramatically by using a modified fluctuation-response relation derived by Speck and Seifert (30).

It is suggested that imperfect arrangement of the quadrupolar electrodes and imperfect balance of the voltage amplitude appends an angular dependency to the electrorotation torque and causes an artificial barrier at the stall to reverse the rotation (8, 20–22, 31). The effect is incorporated by using angular dependent calibration coefficient $\alpha(\theta) = \alpha_0[1 + \alpha_1(\theta)]$. As we will see, the angular bias $\alpha_1(\theta)$ was typically too small to cause a significant effect on the TS curve. Nevertheless, we estimated $\alpha_1(\theta)$ for eliminating the artefact as far as possible. This was possible by reasonably assuming that only $\alpha_1(\theta)$ has an angular dependency.

We changed the external torque from positive (assisting) to negative (hindering) at a constant rate (Fig. 2a) while superposing 1000-Hz sinusoidal small torque for *in situ* torque calibration (Fig. 2b). By analyzing the rotational trajectories, we recovered γ , α_0 , $\alpha_1(\theta)$ and $T_m(\omega)$ of individual flagellar motors.

2 RESULTS

2.1 Test with simulated trajectory

The validity of our methodology was first tested with a trajectory generated by a numerical simulation based on Langevin equation (14). We used an upper-convex $T_m(\omega)$ with a “knee” at 200 Hz (Fig. 3a). An angular bias $\alpha_1(\theta) = A \cos(\theta)$ with $A = 0.2$ was imposed (Fig. 3f) to simulate the elliptic electrorotation profile. In the experiments below, the bias strength was typically less than 0.1.

We varied V_{sq} from positive (assisting) to negative (hindering) at a constant rate (Figs. 2a and 3b (inset)) with a superposed 1000-Hz sinusoidal torque for estimating α_0 . From the fluctuation and response spectra (Fig. 3e), we recovered γ (Fig. 3c) and α_0 (Fig. 3d). γ and α_0 exhibited similar patterns because the noise in determining γ is dominant in the estimation error of α_0 (see (10) for the relation between γ and α_0). The green curve in Fig. 3a is the motor torque without subtracting the effect of

angular bias $\alpha_1(\theta)$. We observed a barrier at the stall and an offset from the theoretical curve caused by $\alpha_1(\theta)$ (8, 20, 21, 31). The barrier was negligible when the amplitude of $\alpha_1(\theta)$ is less than 0.1 (Fig. 3a (inset)). Finally, we recovered T_m (Fig. 3a) and $\alpha_1(\theta)$ (Fig. 3f) successfully. This demonstrates the validity of our experimental and analytical methodology.

2.2 Torque-speed curves of wild-type motors

The method was next applied to experiments of wild-type motors. A typical result is shown in Fig. 4.

The TS curves reached the stall and the zero-load state, which are not reachable by a viscous load. A plateau from the stall to ca. 200 Hz and relatively steep reduction in torque up to ca. 300 Hz was observed (Fig. 4a), which is consistent with previous reports (9, 10, 13, 16).

We observed a steep rise when the TS curve approaches the stall as observed previously (Fig. 4a) (8, 20–22, 31). Such a steep rise was thought to be an artefact due to the elliptic electrorotation profile with a stronger torque in a specific direction. However, the angular bias was typically less than 10% (Fig. 4f), which is not enough to produce the high stall barrier observed (see inset of Fig. 3a). Actually, the subtraction of the angular bias did not affect the TS curve significantly (Fig. 4a).

It was rarely possible to reverse the rotation due to a large barrier at the stall. Even if the rotation was reversed, motors were often broken and exhibited abnormal rotations as shown previously (8, 20, 21, 23). The motors were also easily broken when the rotation is assisted beyond the zero-load region. Therefore, the TS characteristic was not fully explored in these regions.

Typically, γ was smaller at higher V_{sq} (Fig. 4c). This is possibly because the electric field induces not only a rotational torque but also a dielectric electrophoresis force that pulls the cell apart from the glass surface towards the electrodes. This reduces γ because of the smaller rotation radius and less surface effect (32). On the other hand, α_0 did not have a significant V_{sq} dependency (Fig. 4d).

In Fig. 5a, TS curves of 32 wild-type motors are superposed. By connecting the average of intersection points of the torque-speed curves and the straight lines passing through the origin, we recovered an averaged torque-speed curve, which simulated the averaging procedure in the beads assay (Fig. 5b). The angular bias was also superposed in Fig. 5c.

2.3 Tethered cell assay in the absence of electrorotation

To validate the torque rising near the stall observed in the electrorotation experiments (Fig. 5), independent tethered cell experiment was performed in the absence of the electrorotation. We added a polymer Ficoll at different concentrations to control the viscosity and obtained a TS curve by measuring the rotation rate (Fig. 5b). The torque increase near the stall was reproduced, supporting the existence of the torque barrier to reverse the rotation.

The data obtained here was also used to test the validity of γ estimation. We calculated γ by two different methods; from the fluctuation spectra (γ_f) and from the geometric shape (γ_g) (Fig. 5d). Although γ_g calculation contains an unknown geometric parameter h (13), the distance between the cell body and the glass surface, a clear correlation between γ_f and γ_g was observed, supporting the validity of the present estimation of γ .

2.4 Torque-speed curves of mutant motors

The method was applied to a stator-less mutant to validate the method. The stator-less mutant lacks the stator units MotA and MotB and does not generate torque. The TS curves of the stator-less mutant distributed around zero (Fig. 6a) with standard deviations typically less than 100 pN nm/rad, which corresponds to the accuracy of the method. The deviation was larger for higher external torque. This is because, with a higher external torque, T_m is obtained by subtracting a large value of αV_{sq} from a large value of $\gamma \omega$ (3), causing a large statistical error.

We also applied the method to two *Salmonella* mutants having a point mutation in stator proteins: MotA(M206I) (33) and MotB(D33E) (12) (Fig. 6). MotA(M206I) is known to have a smaller proton binding rate (34). Since the low-load, high-speed regime of TS curve depends on the proton translocation (16), it is expected that the mutant has a smaller zero-load rotation rate while the stall torque is unchanged significantly. On the other hand, MotB(D33E) mutant is known to have a smaller stall torque and also a smaller zero-load rotation rate (12). This is possibly due to a smaller proton translocation rate than the wild-type motors. The recovered TS curves of these mutants exhibited the expected characteristics of the motors (Fig. 6b-e).

3 DISCUSSION AND CONCLUSION

We developed the calibration of electrorotation method and applied it to the flagellar motors. The torque magnitude generated by the motor was measured *in situ* under dynamically controlled external load. By sweeping external torque at a constant rate, we recovered the torque-speed curves of individual wild-type motors (Figs. 4 and 5), stator-less mutant motors (Fig. 6a), and smaller-torque mutant motors (M206I and D33E, Fig. 6b-e).

The method showed a steep increase in the motor torque as the TS curve approaches the stall. The existence of the steep rise is, however, controversial. Such a barrier was reported in the previous electrorotation experiments using *E. coli* (8, 20–22). They concluded that this is due to the artefact caused by an imperfect electrode arrangement, supported by the fact that such a barrier was not observed in an experiment with a tethered *E. coli* cell loaded by optical tweezers(31). In the present set up, the effect of angular dependency was small (Fig. 5c). Furthermore, we recovered the TS curve with eliminating this artefact and still had a large barrier (Figs. 4a and 5a and b). In addition, we reproduced the steep rise by independent conventional tethered cell assay under various viscosities (Fig. 5b). These results imply that the steep rise may indeed reflect the motor property at least in our system with *Salmonella*. This steep rise, or a barrier to reverse the rotation, is a characteristic of a ratchet-type torque generation, indicating the existence of a rate limiting step not accompanied by a rotation (22). We also observed an upper-convex TS profile with a knee, which is a characteristic of a power-stroke-type torque generation, at the same time. This suggests that the flagellar motor exploits a combined mechanism of the ratchet and power stroke.

However, such a barrier has not been reported previously in the beads assay of *Salmonella* (3, 10, 12, 13, 16). This discrepancy implies that the assay configuration may alter the rate limiting step. The environment for the motor of the tethered cell could be different from the motor in the beads assay by an unknown factor. For example, the distribution and state of protons in a narrow gap between the motor and the charged glass surface can be significantly different from those of the bulk protons, possibly affecting the proton motive force and the proton flow kinetics, leading to the alternation of the rate limiting step in the motor cycle.

Thus, though more detailed studies are necessary to resolve this intriguing discrepancy, the methodology demonstrated here would add a new dimension to the study of bacterial flagellar motors. For example, it provides a powerful tool to investigate the load-dependent change in the number of docked stator units (5–7, 9, 35–38) by probing the motor torque change upon a temporal load change. In the present experiment, we did not observe a clear sign of such stator association with and dissociation from the motor in the rotational trajectories. One possible reason is that the 30-s duration of the present torque sweeping might be too short to observe such events with the time scale of about one minute(37). Although the TS curves of individual motors were obtained, a distinct motor individuality was not identified in the present experiment. A future challenge with improved system and more systematic statistical analysis may reveal the individualities.

This work was supported by JSPS KAKENHI (16H00791). We thank Yuya Suzuki for preparing the plasmids.

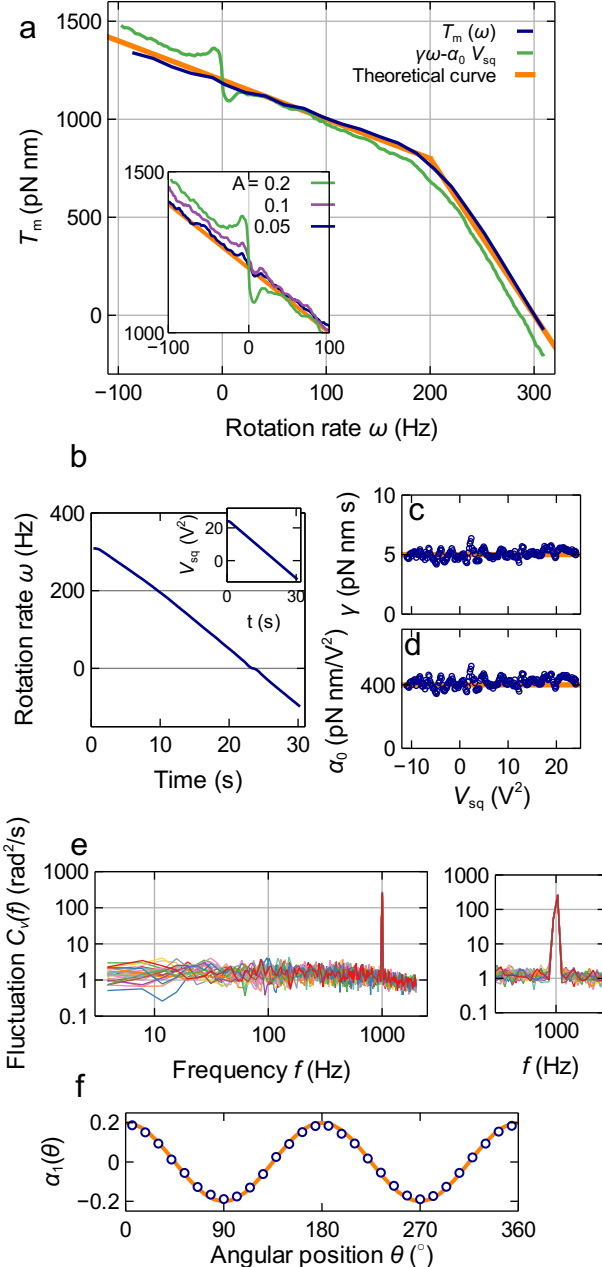


Figure 3: Test of the method with a simulated trajectory. **a**, Recovered TS curve $T_m(\omega)$ (blue) for a postulated upper-convex polygonal profile (orange). Green curve is $\gamma\omega - \alpha_0 V_{sq}$. An angular bias $\alpha_1 = A \cos(2\theta)$ with $A = 0.2$ was imposed. Inset: $\gamma\omega - \alpha_0 V_{sq}$ with different strength of angular bias. **b**, Rotational rate generated by a simulation based on Langevin equation. V_{sq} was changed linearly in time (Inset). A pause is observed at the stalled state due to the barrier imposed by $\alpha_1(\theta)$. **c, d**, Estimation of the rotational frictional coefficient γ (**c**) and the calibration coefficient α_0 (**d**). **e**, Fluctuation spectra of the rotational velocity. Spectra of every 20 windows were shown. **f**, Recovered $\alpha_1(\theta)$. Orange curves in **a, c, d**, and **f** indicate the theoretical values used in the simulation.

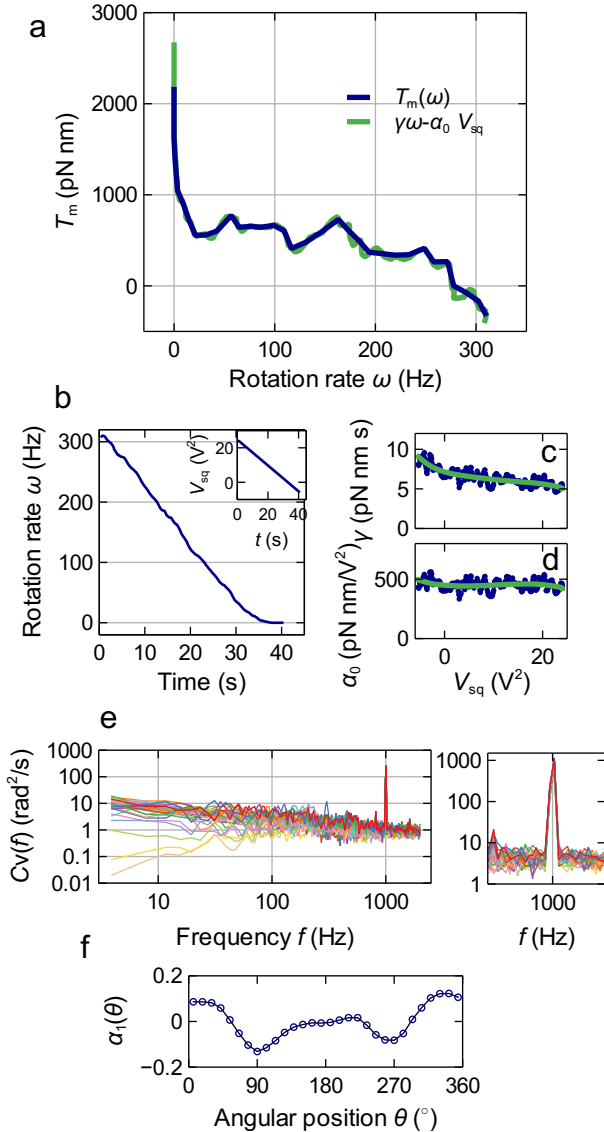


Figure 4: Typical result of a wild-type motor. **a**, $T_m(\omega)$ (blue) and $\gamma\omega - \alpha_0 V_{sq}$ (green). **b**, Rotational rate under a sweeping external torque. **c**, The frictional coefficient γ . **d**, The calibration coefficient α_0 . Solid curves in **c** and **d** are smoothed curves. **e**, Fluctuation spectra of the rotational velocity. Spectra picked every 20 windows were shown. **f**, $\alpha_1(\theta)$.

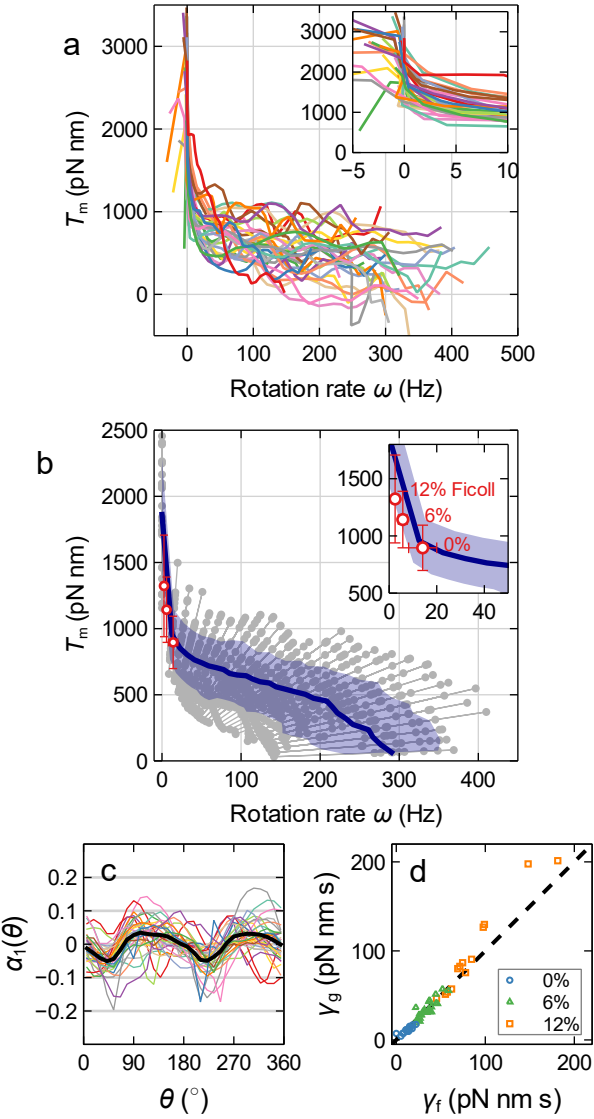


Figure 5: Torque-speed curves of wild-type motors. **a**, TS curves of 32 wild-type motors were superposed. Inset: magnification around the stalled state. **b**, Average of the TS curves in **a** is made in the similar way to the beads assay analysis. Gray circles are the intersections between the TS curves of individual motors and straight lines $T_m(\omega) = a\omega$ with varying slope a . The averaging is done only in the quadrant of $\omega > 0$ and $T_m > 0$ because this analysis is only effective in that region (see main text). Blue thick curve is the mean in the load windows, simulating the beads assay experiments, with the shadow indicating the magnitude of the standard deviation. Red circles are torque-speed curves measured by a tethered cell assay in a Ficoll solution without electrorotation. The frictional coefficient calculated from the geometric shape γ_g was used to calculate the motor torque. Error bars indicate the standard deviations. The sample counts were 17 (0% (w/v) Ficoll), 24 (6%), and 12 cells (12%). Data outside 2σ were omitted from averaging. **c**, Angular bias $\alpha_1(\theta)$ estimated for the motors in **a** are superposed. Black think line is the mean. **d**, Comparison between the frictional coefficient γ of the tethered cell assay calculated from the fluctuation (γ_f) and that from geometric shape parameters (γ_g) in MOPS buffer (circle), 6% Ficoll solution (triangle), and 12% Ficoll solution (square). Thick line corresponds to $\gamma_g = \gamma_f$. We calculated γ_g with the distance between the cell body and the glass surface $h = 250$ nm. See Methods for details.

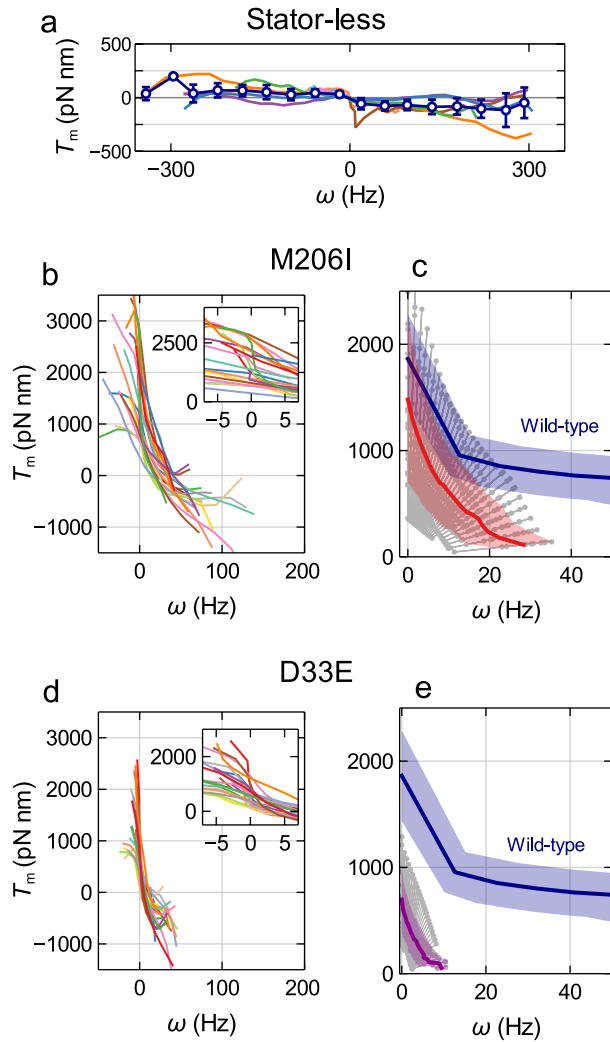


Figure 6: Torque-speed curves of mutants. **a**, TS curves of 10 Δ MotA/B motors. The blue thick line is the average in windows of 40 Hz with the standard deviation as the error bars. **b, c**, MotA(M206I) motor. TS curves of 23 motors were superposed in **b**, **e**, MotB(D33E) motor. TS curves of 22 motors were superposed in **d**. See Fig. 5 for the curve plots. Thick blue lines in **c** and **e** indicate the TS curve of wild-type motors as a guide (Fig. 5b).

4 MATERIALS AND METHODS

4.1 Bacterial strain

Salmonella strain YSC2123, which lacks *motA*, *motB*, *cheY*, *fimA*, and *fliC* (204–292), was transformed with a plasmid encoding wild-type *motA/motB*, *motA*(M206I)/*motB*, or *motA*/*motB*(D33E) (15, 39, 40). L-broth was prepared as described previously (41). A solution of 10 mM MOPS(3-Morpholinopropanesulfonic acid) and 10 mM KCl adjusted to pH7.0 with KOH was used as an observation buffer.

4.2 Electrorotation method

Observation chamber has quadrupolar electrodes with a spacing of 50 μm on the surface of the bottom glass slide. After a 10- μl droplet of the cell solution was placed at the center of the electrodes, a cover slip (Matsunami, Japan) was placed with a thin both-side adhesive tape (10 μm thickness, Teraoka, Japan) as a spacer. Only the top of the both-side adhesive tape was coated by a high-vacuum grease (Shin-Etsu, Japan) so that the top cover slip can be moved. This enables us to move the cells tethered on the top glass slip into the center of the electrodes. After 3 minutes, 20 μl of the observation buffer, and then, 10 μl of blocking buffer (observation buffer containing 50 mg/ml Perfect Block (MobiTec, Germany)) were flew into the chamber. After 2 minutes, 20 μl of the observation chamber was flew into the chamber to wash free Perfect Block.

For tethered cell assays, cells were grown in L-broth containing 100 $\mu\text{g}/\text{ml}$ ampicillin for 5 hours at 30°C with shaking; 0.002% arabinose was added and then incubated for 30 minutes at 30°C with shaking for protein expression (except the stator-less mutant experiments in Fig. 6a). After replacement of L-broth with the observation buffer, we partially sheared the sticky flagella filaments by passing the bacterial solution through 25G needle 70 times. We observed the rotation of a tethered cell at a room temperature (24°C) on a phase-contrast upright microscope (Olympus, Japan) with a 60 \times objective lens (Olympus, NA=1.42), at 4,000 Hz using a high-speed CMOS camera (Basler, Germany), high-intensity LED (623 nm, 2.5W, Thorlabs, NJ) for illumination, and a laboratory-made capturing software developed on LabVIEW 2014 (National Instruments, TX). The angular position of the cellular body was analysed by an algorithm based on a principal component analysis of the cell image. This method reduces the instrumental noise compared to the centroid-based method.

A 10-MHz sinusoidal voltage with a phase shift of $\pi/2$ was induced on the four electrodes. The signal was generated by a function generator (nf, Japan) controlled by PC and amplified by two voltage amplifiers (nf). The amplified voltages were divided by 180° phase distributors (Thamway, Japan) and loaded on the electrodes. This generates an electric field rotating at 10 MHz in the center of the electrodes and induces a dipole moment rotating at 10 MHz on the cell body. Since there is a phase delay between the electric field and dipole moment, the cell body is subjected to a constant torque. The magnitude of torque is proportional to the square of the voltages' amplitude V_0 and the volume of the cell body. We modulated V_0 by a signal generated by the multifunction board (National Instruments) equipped on PC. The camera and amplitude signal were synchronized at a time difference less than one microsecond.

4.3 Measurement of γ and α_0

We controlled the magnitude and sign of the torque by varying the amplitude of the applied voltage V_0 and the phase shift between the electrodes. The torque (N) is proportional to the square of the voltages' amplitude (V_0): $N \equiv \alpha_0 V_{\text{sq}}$, where $V_{\text{sq}} = V_0^2$ or $-V_0^2$ depending on the sign of the phase shift ($\pi/2$ or $-\pi/2$). As noted, α_0 depends on multiple quantities and is not known *a priori*. In this study, we developed the calibration method of α_0 reported in the previous work including the angular dependency (25, 27) further to apply it to the tethered cell assay.

When we look at the rotations in the frequency space, the rotations by the motor is limited to the low frequency region (24). On the other hand, the high frequency region exhibits an equilibrium Brownian motion. When the system is close to the equilibrium state, the fluctuation-response relation holds. This relation connects the fluctuation $\tilde{C}(f)$ and the response to a small perturbation $\tilde{R}'(f)$:

$$\tilde{C}(f) = 2k_{\text{B}}T\tilde{R}'(f). \quad (4)$$

Here, $\tilde{C}(f)$ is the Fourier transform of the auto-correlation function of the rotational velocity $C(t) = \langle \omega(\tau + t)\omega(\tau) \rangle$ at a frequency f . For an equilibrium Brownian movement, γ is obtained by

$$\tilde{C}(f) = 2D = \frac{k_{\text{B}}T}{\gamma}. \quad (5)$$

Here, D is the diffusion coefficient.

On the other hand, $\tilde{R}'(f)$ is the response to a small torque at a frequency f . $\tilde{R}'(f)$ is the real part of the Fourier-Laplace transform of the linear-response function $R(t) : \langle \omega(t) \rangle_{\text{N}} = \omega_0 + \int_{-\infty}^t ds R(t-s)N(s)$, where $\langle v(t) \rangle_{\text{N}}$ denotes the ensemble average

of the rotational velocity under a sufficiently small probe torque $N(t)$. $\omega_0 \equiv \langle \omega(t) \rangle_0$ is the mean rotational velocity in the absence of external torque. Because of the causality, $R(t) = 0$ if $t < 0$. Given that we apply a sufficiently small sinusoidal torque $N(t) = N_0 \sin(2\pi f_0 t)$ of a frequency f_0 and obtain a velocity profile $\langle \omega(t) \rangle_N = \omega_0 + w_0 \sin(2\pi f_0 t + \phi)$, it is easily shown that $\tilde{R}(f_0)$ becomes

$$\tilde{R}(f_0) = \frac{w_0}{N_0} e^{i\phi}. \quad (6)$$

Note that w_0 and ϕ depend on f_0 . By measuring the response (w_0 and ϕ) and fluctuation ($\tilde{C}(f_0)$) of the rotational velocity at sufficiently high frequency f_0 , α_0 is obtained from (4), (6), and $N_0 = \alpha_0 V_{\text{sq}}$:

$$\alpha_0 = 2k_B T \frac{w_0 \cos \phi}{V_{\text{sq}} \tilde{C}(f_0)} = \frac{2w_0 \cos \phi}{V_{\text{sq}}} \gamma. \quad (7)$$

However, we used $\tilde{C}_v(f)$ and $\tilde{R}'_v(f)$ for $\tilde{C}(f)$ and $R'(f)$. See the next section.

4.4 Angular dependency of α

As we seen in Fig. 5c, the magnitude of the electrorotation has a small angular dependency. This causes the following two effects on the TS curve recovery.

First, the periodic perturbation causes a periodic variation of the rotation rate with the frequencies equal to the integral multiple of the mean rotation rate. These can produce nonequilibrium fluctuation at more than 1,000 Hz and affects the above torque calibration. This has not been a problem with the F₁-motor (25, 27), which rotates at much lower rotation rate. Also, because the cell body is relatively large compared the probe used for the F₁-motor, the spectrum intensity is small at high frequencies due to the large γ (see (5)) and suffered much from the noise.

However, such the nonequilibrium fluctuations can be eliminated by using the modified fluctuation-response relation proposed by Speck and Seifert (29, 30).

$$\tilde{C}_v(f) = 2k_B T \tilde{R}'_v(f). \quad (8)$$

Here, $\tilde{C}_v(f)$ and $\tilde{R}'_v(f)$ are the fluctuation and response function of the rotation rate around the local mean velocity defined as

$$\omega_v(t) \equiv \omega(t) - v(\theta(t)), \quad (9)$$

where $v(\theta_0) = \int_0^T dt \delta(\theta(t) - \theta_0) \omega(t)$ is the local mean velocity, and $\theta(t)$ is the angular position at time t . $\delta(x)$ is the Dirac's delta function. That is, $v(\theta)$ is the mean rotation rate at the angular position θ . $v_v(t)$ is the rotational rate subtracted by the local mean velocity at each location. That is, the fluctuation due to a stationary periodic potential is subtracted. $C_v(t) = \langle \omega_v(\tau + t) \omega_v(\tau) \rangle$ and $\langle \omega_v(t) \rangle_N = \int_{-\infty}^t ds R_v(t - s) N(s)$. The idea behind this is that the fluctuation-response relation is restored for the rotation around the local mean velocity. The nonequilibrium rotations are embedded in the local mean velocity (29).

Throughout this work, we used $\tilde{C}_v(f)$ and $\tilde{R}'_v(f)$ instead of $\tilde{C}(f)$ and $R'(f)$ to eliminate the effect of the periodic potential for calculating γ and α_0 :

$$\gamma = \frac{k_B T}{\tilde{C}_v(f_0)}, \quad \alpha_0 = \frac{2w_0 \cos \phi}{V_{\text{sq}}} \gamma. \quad (10)$$

Second, the angular dependency of electrorotation torque $\alpha_1(\theta)$ produces a barrier to the backward rotation at the stalled state (8, 20, 21, 31). Although $\alpha_1(\theta)$ is unknown *a priori*, we can estimate it by reasonably assuming that only $\alpha_1(\theta)$ is the source of the θ dependency of the rotation rate. See the section (4.5) for details.

4.5 Procedure of experiment and analysis

The experiments and analysis were proceeded as follows.

We applied an external torque varied at a constant ramp rate on the tethered cell superposed by a 1000-Hz small sinusoidal torque (Fig. 2a). The trajectory of the rotations was obtained at 4,000 Hz (exposure time = 190 μ s) by video microscopy. γ and α_0 had a dependency on the electrorotation strength possibly due to the pulling force towards the electric field. Therefore, we divided the trajectory into windows with the length of 4,096 frames with 500-frame shifts and calculated γ and α in each window. We averaged $\tilde{C}(f)$ in the ranges close to 1,000 Hz: [850 Hz, 950 Hz] and [1050 Hz, 1150 Hz] to obtain γ . α_0 was calculated at 1,000 Hz by executing a discrete Fourier transform of the rotational trajectory. $\gamma(t)$ and $\alpha_0(t)$ were smoothed by a line fitting (simulation data) or a spline fitting (experimental data) to recover T_m .

The motor torque T_m and the angular bias $\alpha_1(\theta)$ were calculated by an iterative method by reasonably assuming that only $\alpha_1(\theta(t))$ has a dependency on θ . By integration T_m over a finite period of time (0.5 s),

$$\overline{T_m(\omega(t))} = \overline{\gamma(t)\omega(t) - \alpha_0(t)[1 + \alpha_1(\theta(t))]V_{sq}(t)}, \quad (11)$$

where $\overline{f(t)} \equiv \int f(t)dt$. On the other hand, we estimated $\alpha_1(\theta)$:

$$\alpha_1(\theta(t)) = -1 + \frac{-\overline{T_m(\omega(t))} + \gamma(t)\omega(t)}{\alpha_0(t)V_{sq}(t)}. \quad (12)$$

We calculated the mean of the right-hand side of (12) in each angular bin to estimate $\alpha_1(\theta)$ in the first 20000 frames. In this region, the external torque is dominant to determine the rotation behaviour, and we can measure $\alpha_1(\theta)$ at a good accuracy. By iterating (11) and (12) until a sufficient conversion, we obtained T_m and $\alpha_1(\theta)$.

4.6 Freely-rotating tethered cell assay

In Fig. 5b, we compared the TS curves obtained with the electrorotation and the tethered cell assay in medium of various viscosity.

The tethered cell assay was performed in a solution containing a polymer Ficoll to vary the viscosity. We used 0%, 6% and 12% Ficoll PM400 (GE Healthcare, Sweden) solved in the observation buffer. The viscosity measured by a vibratory viscometer (A&D, Japan) was 0.83 (0% Ficoll), 3.07 (6%), and 7.18 mPa s (12%), respectively, which are similar to the values reported previously (13). The frictional coefficient was calculated as (42)

$$\gamma = \frac{4\pi\eta}{3} \cdot \frac{L_1^3 + L_2^3}{\ln(2(\frac{h}{r} + 1))}. \quad (13)$$

Here, $2r$ is the width of the cell, L_1 and L_2 are the distances between the rotation center and the cellular ends. These values were estimated by analysing the cell image in the phase contrast illumination. We assumed the unknown parameter h , the distance from the chamber surface to the cellular surface, to be 250 nm, which yielded the similar values to those obtained by fluctuation analysis (Fig. 2c).

4.7 Numerical simulations

We solved a Langevin equation numerically

$$\gamma\omega(t) = T_m(\omega(t)) + \alpha_0[1 + \alpha_1(\theta)]V_{sq}(t) + \xi(t), \quad (14)$$

where $\xi(t)$ is a thermal fluctuating torque and satisfies $\langle \xi(t)\xi(0) \rangle = 2\gamma k_B T \delta(t)$. $\delta(t)$ is the Dirac's delta function. $V_{sq}(t)$ simulates the electrorotation. We calculated trajectories $\theta(t)$ for a torque-speed curve with a stall torque of 1200 pN nm/rad, a zero-torque speed of 300 Hz and a “knee” at 200 Hz and 800 pN nm/rad. $\gamma = 5$ pN nm s, $\alpha_0 = 400$ pN nm/V², and $\alpha_1(\theta) = A \cos(2\theta)$ with $A = 0.05, 0.1$, or 0.2 . The trajectories were integrated in 190- μ s windows at 4000 Hz to simulate experimental conditions.

REFERENCES

1. Berg, H. C., 2003. The rotary motor of bacterial flagella. *Annu Rev Biochem.* 72:19–54.
2. Berry, R. M., and J. P. Armitage, 1999. The bacterial flagella motor. *Adv Microb Physiol.* 41:291–337.
3. Sowa, Y., and R. M. Berry, 2008. Bacterial flagellar motor. *Q. Rev. Biophys.* 41:103–132.
4. Nirody, J. A., Y.-R. Sun, and C.-J. Lo, 2017. The biophysicist's guide to the bacterial flagellar motor. *Adv. Phys. X* 2:324–343.
5. Tipping, M. J., N. J. Delalez, R. Lim, R. M. Berry, and J. P. Armitage, 2013. Load-Dependent Assembly of the Bacterial Flagellar Motor. *mBio* 4:00551–13.
6. Fukuoka, H., T. Wada, S. Kojima, A. Ishijima, and M. Homma, 2009. Sodium-dependent dynamic assembly of membrane complexes in sodium-driven flagellar motors. *Mol. Microbiol.* 71:825–835.

7. Lele, P. P., B. G. Hosu, and H. C. Berg, 2013. Dynamics of mechanosensing in the bacterial flagellar motor. *PNAS* 110:11839–44.
8. Berg, H. C., and L. Turner, 1993. Torque Generated by the Flagellar Motor of *Escherichia coli*. *Biophys. J.* 65:2201–2216.
9. Ryu, W. S., R. M. Berry, and H. C. Berg, 2000. Torque-generating units of the Flagellar motor of *Escherichia coli* have a high duty ratio. *Nature* 403:444.
10. Chen, X., and H. C. Berg, 2000. Torque-Speed Relationship of the Flagellar Rotary Motor of *Escherichia coli*. *Biophys. J.* 78:1036–41.
11. Sowa, Y., H. Hotta, M. Homma, and A. Ishijima, 2003. Torque-speed Relationship of the Na^+ -driven Flagellar Motor of *Vibrio alginolyticus*. *J. Mol. Biol.* 327:1043–51.
12. Che, Y.-S., S. Nakamura, S. Kojima, N. Kami-ike, K. Namba, and T. Minamino, 2008. Suppressor Analysis of the MotB(D33E) Mutation To Probe Bacterial Flagellar Motor Dynamics Coupled with Proton Translocation. *J. Bact.* 190:6660–7.
13. Castillo, D. J., S. Nakamura, Y. V. Morimoto, Y.-S. Che, N. Kami-ike, S. Kudo, T. Minamino, and K. Namba, 2013. The C-terminal periplasmic domain of MotB is responsible for load-dependent control of the number of stators of the bacterial flagellar motors. *biophysics* 9:173–181.
14. Inoue, Y., C.-J. Lo, H. Fukuoka, H. Takahashi, Y. Sowa, T. Pilizota, G. H. Wadhams, M. Homma, R. M. Berry, and A. Ishijima, 2008. Torque-Speed Relationships of Na^+ -driven Chimeric Flagellar Motors in *Escherichia coli*. *Biophys. J.* 376:1251–1259.
15. Che, Y.-S., S. Nakamura, Y. V. Morimoto, N. Kami-ike, K. Namba, and T. Minamino, 2014. Load-sensitive coupling of proton translocation and torque generation in the bacterial flagellar motor. *Mol. Biol.* 91:175–184.
16. Nakamura, S., N. Kami-ike, P. J. Yokota, S. Kudo, T. Minamino, and K. Namba, 2013. Effect of intracellular pH on the torque-speed relationship of bacterial proton-driven flagellar motor. *J. Mol. Biol.* 386:332–338.
17. Brenner, H., 1961. The slow motion of a sphere through a viscous fluid towards a plane surface. *Chem. Eng. Sci.* 16:242–251.
18. Iwazawa, J., Y. Imae, , and S. Kobayashi, 1993. Study of the torque of the bacterial flagellar motor using a rotating electric field. *Biophys. J.* 64:925–933.
19. Washizu, M., Y. Kurahashi, H. Iuchi, O. Kurosawa, S. Aizawa, S. Kudo, Y. Magariyama, and H. Hotani, 1993. Dielectrophoretic measurement of bacterial motor characteristics. *IEEE Trans. Ind. Appl.* 29:286.
20. Berry, R. M., L. Turner, and H. C. Berg, 1995. Mechanical limits of bacterial flagellar motors probed by electrorotation. *Biophys. J.* 69:280–286.
21. Berry, R. M., and H. C. Berg, 1996. Torque Generated by the Bacterial Flagellar Motor Close to Stall. *Biophys. J.* 71:3501.
22. Berry, R. M., and H. C. Berg, 1999. Torque Generated by the Flagellar Motor of *Escherichia coli* while Driven Backward. *Biophys. J.* 76:580–587.
23. Sugiyama, S., Y. Magariyama, and S. Kudo, 2004. Forced rotation of Na^+ -driven flagellar motor in a coupling ion-free environment. *BBA* 1656:32.
24. Toyabe, S., T. Okamoto, T. Watanabe-Nakayama, H. Taketani, S. Kudo, and E. Muneyuki, 2010. Nonequilibrium energetics of a single F_1 -ATPase molecule. *Phys. Rev. Lett.* 104:198103.
25. Toyabe, S., T. Watanabe-Nakayama, T. Okamoto, S. Kudo, and E. Muneyuki, 2011. Thermodynamic efficiency and mechanochemical coupling of F_1 -ATPase. *Proc. Nat. Acad. Sci. USA* 108:17951–17956.
26. Toyabe, S., and E. Muneyuki, 2013. Experimental thermodynamics of single molecular motor. *Biophys.* 9:91–98.
27. Toyabe, S., and E. Muneyuki, 2015. Single molecule thermodynamics of ATP synthesis by F_1 -ATPase. *New J. Phys.* 17:015008.

28. Kubo, R., M. Toda, and N. Hashitsume, 1991. *Statistical Physics II*. Springer, Berlin, second edition.
29. Toyabe, S., and M. Sano, 2015. Nonequilibrium Fluctuations in Biological Strands, Machines, and Cells. *J. Phys. Soc. Jpn.* 84, 102001 (2015). 84:102001.
30. Speck, T., and U. Seifert, 2006. Restoring a fluctuation-dissipation theorem in a nonequilibrium steady state. *EPL* 74:391.
31. Berry, R. M., and H. C. Berg, 1997. Absence of a barrier to backwards rotation of the bacterial flagellar motor demonstrated with optical tweezers. *PNAS* 94:14433–14437.
32. Leach, J., H. Mushfique, S. Keen, R. Di Leonardo, G. Ruocco, J. M. Cooper, and M. J. Padgett, 2009. Comparison of Faxén's correction for a microsphere translating or rotating near a surface. *Phys. Rev. E* 79:026301.
33. Komatsu, H., F. Hayashi, M. Sasa, K. Shikata, S. Yamaguchi, K. Namba, and K. Oosawa, 2016. Genetic analysis of revertants isolated from the rod-fragile fliF mutant of *Salmonella*. *Biophys. Physicobiol.* 13:13–25.
34. Suzuki, Y., Y. V. Morimoto, K. Oono, F. Hayashi, K. Oosawa, S. Kudo, and S. Nakamura, 2018. Proton binding to flagellar motor stators stabilizes their localization around the rotor in *Salmonella*, Submitted.
35. Block, S. M., and H. C. Berg, 1984. Successive incorporation of force-generating units in the bacterial rotary motor. *Nature* 309:470–2.
36. Blair, D. F., and H. C. Berg, 1988. Restoration of torque in defective flagellar motors. *Science* 242:1678–81.
37. Leake, M. C., J. H. Chandler, G. H. Wadhams, F. Bai, R. M. Berry, and J. P. Armitage, 2006. Torque-generating units of the Flagellar motor of *Escherichia coli* have a high duty ratio. *Nature* 443:355.
38. Yuan, J., and H. C. Berg, 2008. Resurrection of the flagellar rotary motor near zero load. *PNAS* 105:1182.
39. Morimoto, Y. V., S. Nakamura, K. D. Hiraoka, K. Namba, and T. Minamino, 2013. Distinct Roles of Highly Conserved Charged Residues at the MotA-FliG Interface in Bacterial Flagellar Motor Rotation. *J. Bact.* 195:474–481.
40. Morimoto, Y. V., Y. S. Che, T. Minamino, and K. Namba, 2010. Proton-conductivity assay of plugged and unplugged MotA/B proton channel by cytoplasmic pHluorin expressed in *Salmonella*. *FEBS Lett.* 584:1268–72.
41. Minamino, T., Y. Imae, F. Oosawa, Y. Kobayashi, and K. Oosawa, 2003. Effect of intracellular pH on rotational speed of bacterial flagellar motors. *J. Bac.* 185:1190–1194.
42. Howard, J., 2001. *Mechanics of Motor Proteins and the Cytoskeleton*. Sinauer Associates, Sunderland.